

Radiative–Convective Feedbacks in Idealized States of Radiative–Convective Equilibrium

GRAEME L. STEPHENS, SUSAN VAN DEN HEEVER, AND LYLE PAKULA

Department of Atmospheric Science, Colorado State University, Fort Collins, Colorado

(Manuscript received 25 May 2007, in final form 9 April 2008)

ABSTRACT

This paper examines feedbacks between the radiative heating of clouds and convection in the context of numerical radiative–convective equilibrium experiments conducted using both 2D and 3D versions of a cloud-resolving model. The experiments are conducted on a large domain, and equilibria develop as juxtaposed regions of dry and moist air that are connected and sustained by circulations between them. The scales of such variability are large and differ significantly between the 2D and 3D versions of the experiments. Three sensitivity experiments were conducted which, when compared to the control experiment, provide insight into the relative influences of cloud–radiation feedback mechanisms on the equilibrium state achieved. It emerges from the experiments conducted that radiation feedbacks operate via two main pathways, with the radiative heating by high clouds being the governing process of both. The predominant bimodal nature of the moist equilibrium is established by gradients in radiative heating that, in turn, are determined by high cloud differences between wet and dry regions that, in turn, are controlled by convection. Convection, on the other hand, is also influenced by the localized effects of cloud radiative heating by these extended layers of high clouds. The results of the experiments demonstrate how high cloud radiative heating, which is a by-product of the convection itself, provides a feedback that acts to regulate the high clouds produced in the wet convective areas of the equilibrium.

1. Introduction

Cumulus convection is essential to many important interactions of the physical climate system (Arakawa 2004) and to the feedback mechanisms that modulate it (Stephens 2005). Not only does convection contribute significantly to the hydrological cycle through the precipitation it produces, but convection is also intimately important to the planet's energy balance. One way to consider the important connections between convection and the energy budget of the earth is through the notion of radiative–convective equilibrium (RCE). This viewpoint is relevant to the climate of the earth because the global-mean state of the planet is thought to exist in a state of RCE. In this state the input to the atmospheric energy budget is heat, transferred from the surface, that is associated with convective processes and large-scale winds. These inputs are balanced by energy

losses from the atmosphere resulting from atmospheric emission of radiation that exceeds its radiation absorption (radiative cooling). In RCE, most of the heat transfer via convection that balances this radiative cooling is due to the latent heating associated with the precipitation of moist convection (e.g., Mitchell et al. 1987). One of the important consequences of such an equilibrium state is exemplified in climate change experiments performed with climate models, in which changes in global precipitation are shown to be forced by changes in atmospheric radiative cooling associated with increased greenhouse gases (e.g., Stephens 2005).

It is for these reasons, among others, that studying the nature of convection in RCE and the feedbacks between radiation and convection is of some relevance to the real climate system. The direct influence of atmospheric radiative cooling on convection has been studied in a number of papers reporting on radiative–convective equilibrium experiments conducted with cloud-resolving models (CRMs). Dudhia (1989) and Robe and Emanuel (1996), for example, confirm that under the state of radiative–convective equilibrium, increased cooling of the atmosphere indeed forces in-

Corresponding author address: Graeme L. Stephens, Department of Atmospheric Science, Colorado State University, Fort Collins, CO 80523-1371.
E-mail: stephens@atmos.colostate.edu

creased convection and associated precipitation. Other studies have gone further and hinted at the importance of: (i) feedbacks on convection via cloud layer destabilization by intense cloud-top cooling (Webster and Stephens 1980; Tao et al. 1996; Xu and Randall 1995), (ii) feedbacks involving secondary circulations forced by differential horizontal radiative heating between cloudy and clear regions (Gray and Jacobson 1977; Raymond 2000; Mapes 2001; Sherwood 1999), and (iii) stabilizing feedbacks associated with upper tropospheric radiative heating by cirrus detrained from convection (Stephens et al. 2004; Fu et al. 1995; Fowler and Randall 1994; etc.).

The purpose of the present paper is to report on simple RCE experiments aimed at elucidating the extent to which the above-mentioned feedback mechanisms operate either individually or in combination to control the nature of convection in such idealized RCE experiments. There is much insight to be gained from the simple experiments performed, given that the factors that organize and influence convection in the real atmosphere, especially on the time scales pertinent to RCE, are not well understood. We explore these feedbacks both with respect to their gross influence on the domain-mean equilibrium reached and with respect to the influence of the feedbacks on the organization of convection within this mean equilibrium state.

The experiments described in this study are conducted using both two- and three-dimensional versions of a particular CRM. Previous RCE studies that employ CRMs reveal spatial distributions of convection that are not quasi-homogenous but are organized into spatial structures with distinct scales of organization. This has led to the notion of self-aggregation (Held et al. 1993; Su et al. 2000; Bretherton et al. 2005), that is, the conjecture that such organization is self-sustaining. Most studies of convective self-aggregation in RCE adopt 2D versions of CRMs, although a limited number 3D experiment results have also been reported (Tompkins and Craig 1998a,b; Bretherton et al. 2005). These and other studies tend to point to the importance of feedbacks involving the connection between water vapor and convection as a process instrumental to self-aggregation (Held et al. 1993; Tompkins 2001; Grabowski and Moncrieff 2004), and Bretherton et al. (2005) show that this aggregation disappears in RCE with the spatial homogenization of surface fluxes. However, many questions raised by such experiments remain unanswered, such as to what extent are the organization and its scale artifacts of the model setup, or to what extent is the scale of aggregation of convection artificially controlled in limited-domain experiments that are unable to capture necessary larger scales of

interaction? Specific concerns also exist over the dimensionality of many of these experiments. For example, the extent to which the convective organization that occurs in 2D experiments may somehow be a consequence of the lack of a third dimension is uncertain. Also, uncertainty exists concerning whether the aggregation that occurs in 3D experiments conducted with domains of limited size (e.g., Robe and Emanuel, 1996; Bretherton et al., 2005) adequately represents processes that occur on much larger scales. This is revealed by the results presented below.

The model used in this study is briefly described in section 2, and the reasons for using a model domain larger than many of the past RCE studies are discussed in section 3, along with other specific details of the experimental setup. Three sensitivity experiments aimed at elucidating the nature the radiative-convective feedbacks important to the RCE state reached by the model are also described in this section. The states of RCE for both the 2D and 3D experiments are described in detail in section 4, and the mean profile structures that characterize these equilibria are introduced in sections 5 and 6. Section 7 provides a discussion and summary of the results and an interpretation of the feedbacks that operate in the different experiments.

2. Model description

The model used in the experiments is the Regional Atmospheric Modeling System (RAMS; Pielke et al. 1992; Cotton et al. 2003) developed at Colorado State University. RAMS is a nonhydrostatic, cloud-resolving model that incorporates sophisticated microphysics, radiation, surface, and turbulence schemes. The model integrates predictive equations for the three wind components, the Exner function, ice liquid potential temperature, and total mixing ratio on a vertically stretched Arakawa C grid. For the simulations conducted here, the surface processes were parameterized using the Land Ecosystem-Atmosphere Feedback model, version 2 (LEAF-2; Walko et al. 2000), turbulence is represented by the Smagorinsky (1963) deformation- K closure scheme with stability modifications by Lilly (1962) and Hill (1974), and the two-stream radiation scheme of Harrington (1997) was called every 5 min.

Although single-moment (Walko et al. 1995) and two-moment (Meyers et al. 1997) bulk microphysical schemes are included in RAMS, only the single-moment scheme is used. Thus, only hydrometeor mixing ratios are predicted by this scheme. All of the available water species (cloud water, rain, pristine ice, snow, aggregates, graupel, hail) are activated for the single-

TABLE 1. Summary of experiments.

Experiment	Model horizontal domain (km)	Radiation assumption
2D CONTROL	$x = 9600$	Fully interactive
3D CONTROL	$x = 9600, y = 180$	Fully interactive
2D FIXRAD	$x = 9600$	Fixed (time and space)
3D FIXRAD	$x = 9600, y = 180$	Fixed (time and space)
2D NO-OPTICS	$x = 9600$	Interactive without contributions by clouds and precipitation
3D NO-OPTICS	$x = 9600, y = 75 \times 2.4$	Interactive without contributions by clouds and precipitation
2D ANVIL	$x = 9600$	Interactive without contributions from any clouds below 8 km

moment experiments conducted here. The cloud droplet spectrum is decomposed into two modes: one for droplets 1 to 40 microns in diameter, and the second for droplets 40 to 80 microns in diameter. This bimodal cloud droplet size distribution permits a more accurate representation of the bimodal droplet distribution that often occurs in the atmosphere. Hydrometeor spectra are represented using a generalized gamma distribution function, the shape parameter of which was set to two for all simulations described here. The collection is simulated using stochastic collection equation solutions, facilitated by look-up tables, rather than by continuous accretion approximations; the bin representation philosophy of collection is extended to calculations of drop sedimentation. Fixed concentrations of aerosol species serve as prognostic variables in RAMS to determine cloud droplet concentrations.

3. Experimental setup

The basic model options and all experiments performed are summarized in Table 1.

a. The model domain

To address concerns about the possible effects of 2D geometry imposing scales of organization of convection that are artificially larger than the characteristic scale of 3D convection (e.g., Tompkins 2000), we conduct experiments in both 2D and 3D. To address concerns about the use of 3D domains restricted to just a few 100 km, we adopt the channel-mode configuration as originally introduced by Tompkins (2001). This configuration represents a compromise between the need for a 3D domain large enough not to trivially constrain the behavior of the convective ensemble and yet small enough to meet the limitations of available computer resources. Differences in the configuration used in this study from that used in Tompkins (2001), however, warrant brief mention. A horizontal grid spacing of 2.4 km is used. Such a grid spacing is typical of that used in other RCE CRM experiments of this type although it only marginally resolves individual deep convective

cores, if at all (e.g., Bryan et al. 2003). This resolution, however, resolves the important mesoscale characteristics of organized convection. The three-dimensional channel experiments employ a domain of 4000 points in the zonal direction and 75 grid points in the meridional direction, thus covering an area of approximately $1\,728\,000\text{ km}^2$ ($9600\text{ km} \times 180\text{ km}$). Except for the ANVIL experiment described below, a matching set of two-dimensional experiments is also analyzed for comparison with the 3D counterparts. These 2D experiments use the same grid spacing and are configured with a domain of 4000 points, resulting in a grid that is 9600 km wide. Both the 2D and 3D experiments use a model with 38 levels in the vertical, eight of which are located within the first kilometer AGL, with the model top extended to approximately 26 km AGL.

b. The control experiments

All experiments were initialized with the 0000 UTC 5 December 1992 Tropical Ocean and Global Atmosphere Coupled Ocean–Atmosphere Response Experiment (TOGA COARE) sounding with initial zero mean wind in the vertical and a fixed and uniform sea surface temperature (SST) of 300 K. The latter remains fixed in the model, whereas the wind field evolves as part of the localized turbulence and broader scale circulations that are established over time. A Rayleigh friction layer was implemented in the top four model levels to absorb gravity waves, and the surface processes were parameterized using the LEAF-2 scheme as noted earlier. Periodic boundary conditions were applied. The Coriolis parameter was set to zero, and the long time step was 10 s. Convection was initiated by randomly perturbing the potential temperature field across the entire domain. The model was integrated out to 55 days and reached equilibrium after about 30 days (refer to Fig. 1, next section). As in past studies of this type, we employ a fixed solar zenith angle of 50° , and thus there is no diurnal cycle representation in this model.

The 2D and 3D control experiments (hereafter 2D CONTROL and 3D CONTROL) were integrated to 55

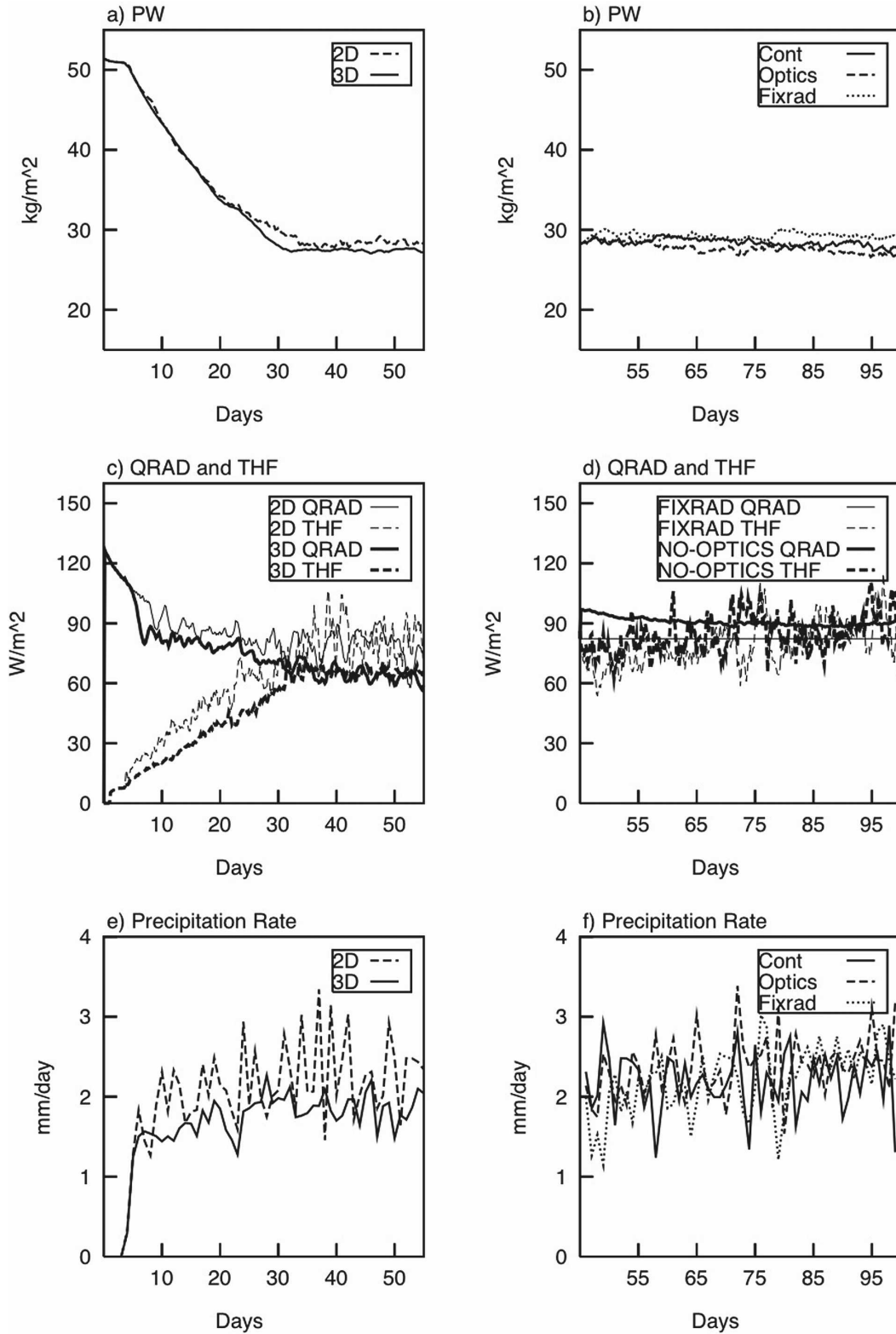


FIG. 1. The time evolution of selected domain-mean quantities depicting (a), (c), (e) the evolution to equilibrium of the control and (b), (d), (f) the 2D sensitivity experiments.

model days and many of the results presented below are derived from the 5 day average between days 45–49.

c. Radiation sensitivity experiments

Two additional 2D and 3D radiation sensitivity experiments, hereafter called the FIXRAD and NO-OPTICS experiments, were performed to examine the feedbacks between radiation and convection. These experiments were initialized in the same way as the control apart from the exceptions now noted. The FIXRAD experiment employs a noninteractive (i.e., fixed in space and time) radiation profile. For this experiment, the domain and time-averaged radiative heating profiles derived from days 40–44 of both control experiments are prescribed at day 45, and thereafter the model is integrated forward with this specified fixed profile. For the NO-OPTICS experiments, the radiative effects of clouds are turned off entirely by setting all cloud optical properties to zero; thus, the localized radiative cooling from cloud top and the cirrus cloud radiative heating are explicitly removed, whereas these radiative effects are contained in the domain-averaged heating profile adopted in the FIXRAD experiment. Given the similarity of the mean RCE state of the 2D and 3D experiments (and given the resources required to integrate the 3D model forward), we integrate the 3D model forward only an additional 10 days (from days 45–55); the 2D model was integrated forward an additional 55 days, thereby guaranteeing a new equilibrium for these experiments.

Differences between the equilibria of the respective control experiments and the FIXRAD experiments highlight the importance of spatial gradients in radiative heating that are established between the moist and dry regions in the control experiments. Differences early on in the integration of both the FIXRAD and NO-OPTICS experiments, represented by the 5-day average over days 40–44, enable examination of the nature of changes in the evolving RCE state and reveal insights on shorter time scale feedbacks. Differences between these experiments and the control reveal the importance of spatial differences in radiative heating. These gradients are primarily a result of the differences in cloudiness between the less convective (undisturbed) regions and the more convective (disturbed) moist regions of the domain. Furthermore, the domain-averaged features of the equilibria achieved in the CONTROL, FIXRAD, and NO-OPTICS experiments are governed by the domain-averaged radiative heating. By construction, these are the same in both the CONTROL and FIXRAD experiments and only marginally different in the NO-OPTICS experiment. The subtle difference in radiative heating profile between

the FIXRAD and NO-OPTICS experiments, however, introduces vastly different influences on the convection that develops early in the model integration. Spatial gradients in radiative heating in the NO-OPTICS experiment, unlike in the FIXRAD experiment, are also established through the existing gradients of water vapor. As we will show, these gradients are too small to induce significant heating differences between the initial wet and dry regions of the domain and are too small to sustain this equilibrium. Eventually the moist–dry equilibrium imposed by the control state breaks down, resulting in a more statistically homogenized state similar to that eventually reached in the FIXRAD experiment.

A third 2D-only experiment, ANVIL, was also performed specifically to demonstrate the effects of the upper tropospheric radiative heating by high clouds on the 2D RCE state. This experiment is a modification of the NO-OPTICS experiment in which the radiative properties of clouds are turned off only below 8 km. Differences between this experiment and both NO-OPTICS and FIXRAD therefore illustrate the specific influence of radiative heating by clouds above 8 km on the convection and the equilibrium.

4. The equilibrium states

a. Evolution to equilibrium

Figures 1a, 1c, and 1e depict the time evolution of the domain average of selected parameters extracted from both the 2D and 3D control experiments, and Figs. 1b, 1d, and 1f provide the same information for the equivalent 2D versions of the FIXRAD and NO-OPTICS experiments. The ANVIL experiment results are not shown in this figure merely for reasons of clarity because the mean quantities derived from the latter experiment lie on top of those shown in Figs. 1b, 1d, and 1f. The parameters shown are the domain-mean column integrated water vapor, or precipitable water (hereafter PW), the thermal (latent plus sensible) heat flux (THF) contrasted against the column net radiative flux divergence (the difference in the net radiative fluxes at the surface and top of atmosphere, Qrad), and the domain-mean precipitation. The time evolution of these quantities reveals much about the gross nature of the equilibrium reached. Multiple time scales, as reported by Tompkins (2000) and noted by others (e.g., Robe and Emanuel 1996), are apparent. A slower time scale representing the approach of the model to an equilibrium state after about 30 days is revealed in the time series of the control PW (Fig. 1a). This time scale is fundamentally set by the time scale of mixing of water vapor in the free troposphere and thus by the time

scale of subsidence (e.g., Tompkins and Craig 1998b), which in turn is largely set by the rate of radiative cooling (e.g., Mapes 2001). Shorter time scale variability is also evident, notably in the precipitation of the 2D control experiment (Fig. 1e). Figures 1b, 1d, and 1f similarly show how the bulk characteristics of the two sensitivity experiments (i.e., the domain means of the quantities selected) are not significantly different than the control and remain stable over the time of integration. However, it is revealed (in Fig. 3) that the structure of the equilibrium undergoes remarkable change as the model is integrated forward to day 95. These changes in structure are not evident in the domain averages of Figs. 1b, 1d, and 1f nor in the domain-averaged profiles discussed later.

At equilibrium, the PW reaches steady levels of 28 kg m^{-2} . The thermal (latent plus sensible) heat flux and radiative flux divergence also come into balance at about 60 W m^{-2} for the 3D experiment and exhibit slightly elevated values in the 2D experiment (approximately 78 W m^{-2}). This equilibrium state of both experiments is dry compared to our expectations of the real atmosphere over 300-K ocean waters. For example, climatological observations suggest that the column water vapor approaches values nearer 40 kg m^{-2} over 300-K ocean waters (e.g., Stephens 1990), and the global-mean precipitation rate is closer to 3 mm day^{-1} , corresponding to latent heat fluxes nearer $80\text{--}90 \text{ W m}^{-2}$ (e.g., Kiehl and Trenberth 1997). The dry state of the equilibrium is mostly a consequence of a combination of the assumed initial resting state of the atmosphere and the way the surface layer fluxes of heat, momentum, and moisture into the atmosphere are parameterized in RAMS. The scheme used in the CRM follows Louis (1979) and Louis et al. (1981) and sets a minimum surface wind speed as the maximum of the surface wind or a parameter v_{\min} , which was taken to be the default value of 0.25 m s^{-1} . Preliminary 2D experiments were conducted with $v_{\min} = 1, 4, \text{ and } 7 \text{ m s}^{-1}$, and a value of $v_{\min} = 4 \text{ m s}^{-1}$ gave mean PW values in line with observations, as in other studies of this type (e.g., Tao et al. 1999).

b. Large-scale structures

We have already noted how the state of RCE in past experiments with CRMs is not one of uniform horizontal structures of temperature and moisture and quasi-homogeneous patterns of cumulus clouds but rather is a state in which moisture and convection are organized. Such organization is portrayed in Figs. 2 and 3 in the form of time–distance (longitude) diagrams. Figure 2 highlights the evolution of PW (top) and outgoing longwave radiation (OLR; bottom) for both the 2D and 3D

control simulations. The 3D simulation results shown were derived for a selected fixed y grid point that corresponds to the center of the domain. Figure 3 presents the 55-day evolution of PW for the CONTROL, FIXRAD, NO-OPTICS, and ANVIL sensitivity experiments from days 46 to 100.

The results of Figs. 2 and 3 demonstrate the wider-scale characteristics of the RCE reached and provide a glimpse of how the water cycle of the model is grossly organized. After an initial spinup of around 10 days, water vapor organizes into distinct dry and moist regions in the control (Fig. 2) that remain more or less coherent and almost stationary over time, as noted in other studies (Held et al. 1993; Tompkins 2001; Grabowski and Moncrieff 2002; etc.). The quasi-stationary moist–dry structures evident in the CONTROL experiments are sustained by circulations that are set up between them (e.g., Grabowski and Moncrieff 2002) and are consistent with the notion of self-aggregation of convection that locks into the wettest areas of the domain, as indicated by the matching organization of OLR.

The coherent moist–dry structures of both the CONTROL and ANVIL experiments show evidence of a very slow propagation on the order of 0.5 m s^{-1} that appears to propagate at first to the left of the domain from day 30 to about day 70 and thereafter to the right of the domain, implying the existence of a mean motion in these experiments. In this and most other respects described below, the ANVIL and CONTROL experiments are similar to each other, thus hinting at the importance of high cloud radiative heating to the equilibrium state reached and the propagation of these organized moist regions. The structure of the PW that develops in the CONTROL experiments is maintained through the first 10 days of the both the NO-OPTICS and FIXRAD experiments in Fig. 3. At this point, the very slowly (almost stationary) propagating moist structures begin to propagate across the domain in both directions with speeds of about $15\text{--}20 \text{ m s}^{-1}$. This propagation is associated with left- and right-moving gravity waves, and the propagation speed is similar to propagating systems both observed in nature (e.g., Tulich et al. 2007) and found in numerical experiments similar to the present study. For example, the FIXRAD and NO-OPTICS results are consistent with the prescribed radiation experiments of Grabowski and Moncrieff (2001), who show systems propagating both to the right and left with speeds varying from 2 to 18 m s^{-1} relative to the applied mean wind in their experiments. The lack of propagation in the CONTROL and ANVIL experiments is also analogous to the interactive radiation experiments of Grabowski and Moncrieff (2002), who

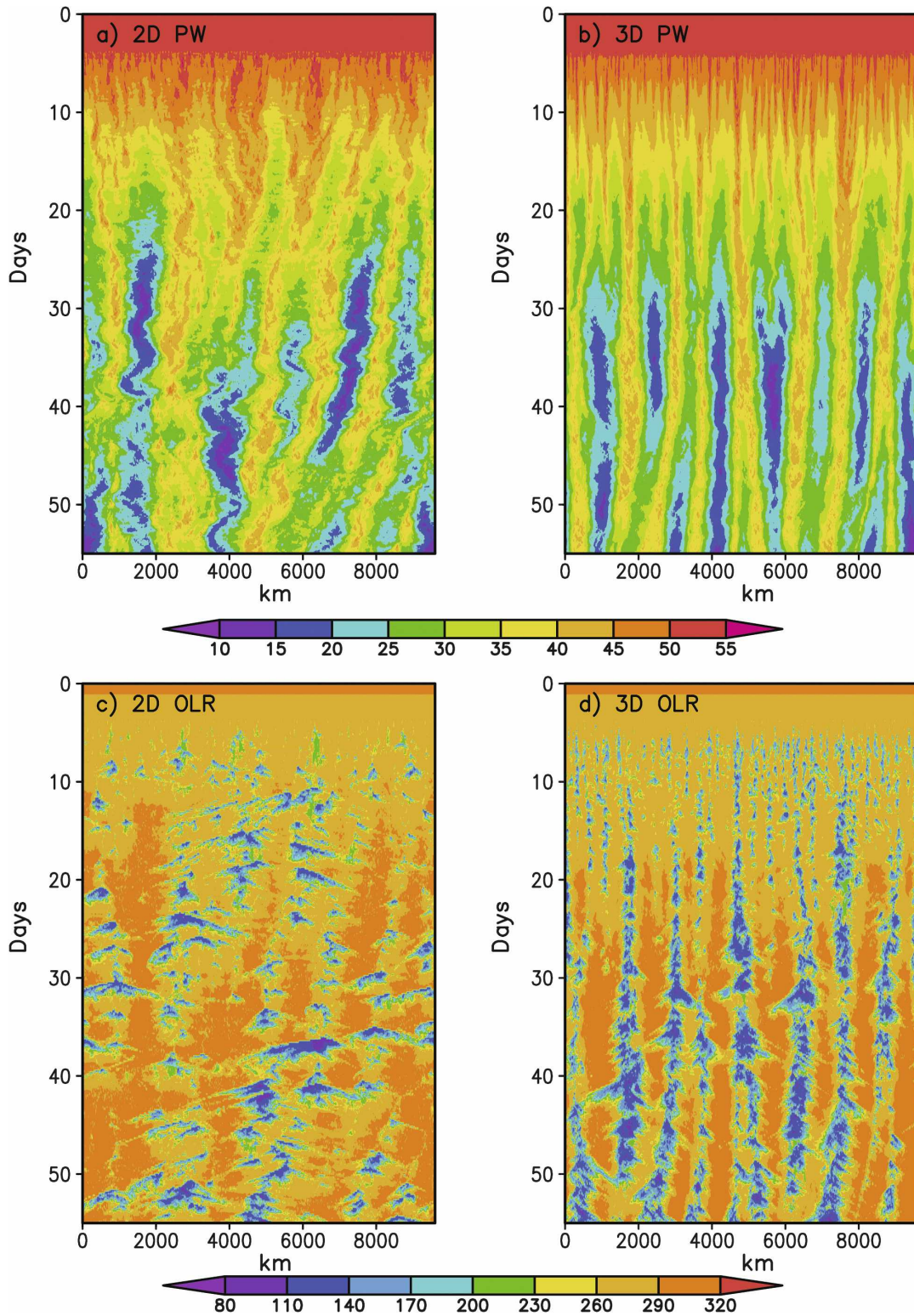


FIG. 2. Hovmöller depiction of the (a), (b) precipitable water (in kg m^{-2}) and (c), (d) OLR (W m^{-2}) for the (a), (c) 2D and (b), (d) 3D control experiments.

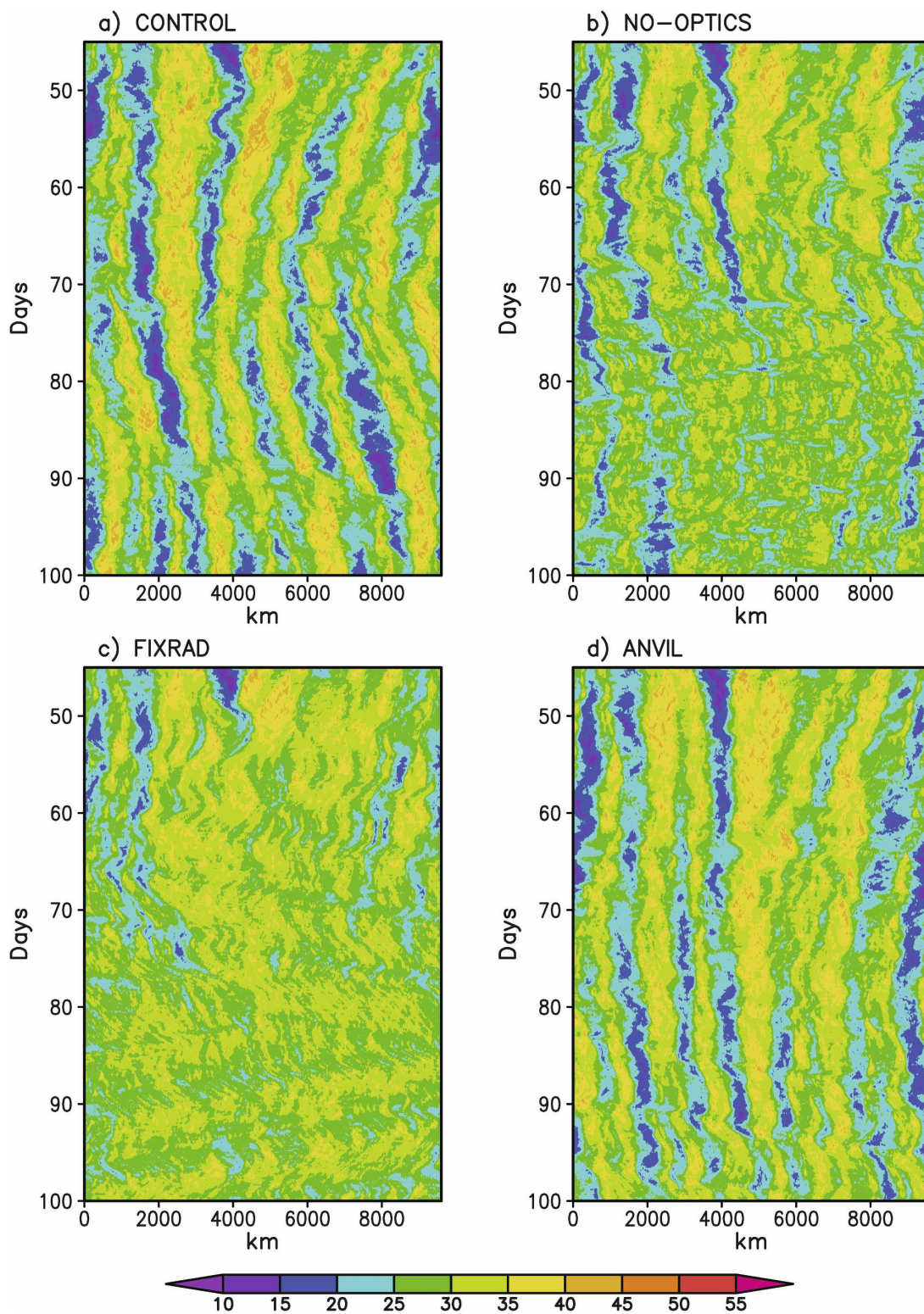


FIG. 3. Hovmöller depiction of the precipitable water (in kg m^{-2}) for the 2D versions of the (a) CONTROL, (b) NO-OPTICS, (c) FIXRAD, and (d) ANVIL experiments for days 46–100.

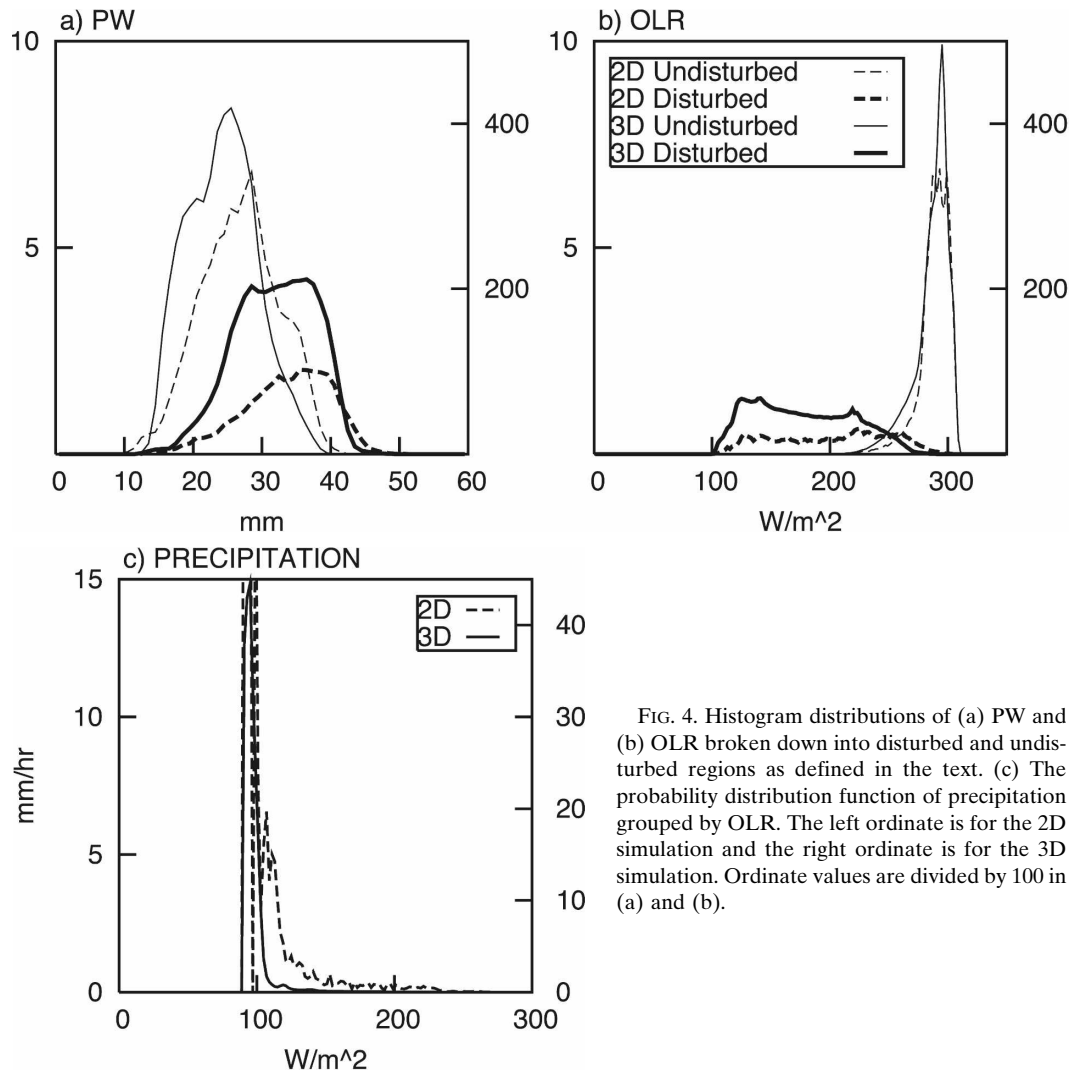


FIG. 4. Histogram distributions of (a) PW and (b) OLR broken down into disturbed and undisturbed regions as defined in the text. (c) The probability distribution function of precipitation grouped by OLR. The left ordinate is for the 2D simulation and the right ordinate is for the 3D simulation. Ordinate values are divided by 100 in (a) and (b).

show similar stationary patterns (relative to the mean prescribed wind in their experiments). Clearly the effects of clouds on the radiative heating and feedbacks on convection, as we discuss below, has an important influence on both the organization and propagation characteristics of convection produced in the experiments shown in Figs. 2 and 3. More detailed studies to address how radiation feedbacks inhibit the propagation of convection and the relevance to convectively coupled waves is a topic of an ongoing study. We note, however, that radiation–moisture feedbacks analogous to those studied in this paper have been shown to influence the phase speeds of the wave solutions of a simple linear analytic model (e.g., Bony and Emanuel 2005). In that model, radiation–moisture feedbacks act to reduce the radiative cooling of the column in regions of wave-induced large-scale ascent, which in turn leads to decreased phase speeds of waves.

Figure 4 provides a slightly different perspective on this moist–dry equilibrium state. Selected quantities are sampled over the 5 days between days 45–49 of the 2D and 3D control experiments to create these non-normalized histograms. These data are composited by grid points that broadly separate areas of near-clear (hereafter “undisturbed”) sky from regions of cloudy (hereafter “disturbed”) sky. The undisturbed regions are defined here as regions for which the path-integrated condensate is less than 0.01 kg m^{-2} and the OLR is greater than 260 W m^{-2} . These regions are thus largely but not entirely free of clouds and are mostly dry, with $PW < 30 \text{ mm}$. The disturbed regions, on the other hand, are regions that contain practically all of the precipitation (Fig. 4c) and high clouds and are characteristically moister than the undisturbed regions (Fig. 4a). The scale of these moist–dry regions also warrants a brief comment, as do the differences in scale between

TABLE 2. Percentage contribution of the three OLR-based regions to domain totals of cloud water path (CWP), ice water path (IWP), surface latent heating (LH), and precipitation (precip).

	Sampling frequency	CWP	IWP	LH	Precip
Deep ($\leq 180 \text{ W m}^{-2}$)					
2D CONTROL	11 747	49	76	11	72
3D CONTROL	1 963 705	76	83	24	87
2D FIXRAD	6144	27	70	6	54
2D FIXRAD days 90–94	72 178	80	98	58	96
3D FIXRAD	860 668	67	82	11	61
Cumulus ($180 \text{ to } 240 \text{ W m}^{-2}$)					
2D CONTROL	13 345	35	17	11	22
3D CONTROL	1 395 059	22	13	16	11
2D FIXRAD	13 017	58	21	12	38
2D FIXRAD days 90–94	15 045	14	2	12	3
3D FIXRAD	844 456	27	12	9	26
Cumulus (240 W m^{-2})					
2D CONTROL	98 846	16	7	78	6
3D CONTROL	5 688 710	2	4	60	2
2D FIXRAD	104 777	15	9	82	8
2D FIXRAD days 90–94	36 715	6	0	30	1
3D FIXRAD	7 342 350	6	6	80	13

the 2D and 3D experiments (e.g., Fig. 2). Simple FFT analysis applied to the average of the last 5 days of both control simulations reveals the dominant scale of PW variability to be approximately 2400 km in the 2D results, compared to a 1200-km scale in the 3D results. Similar analysis of the subsidence indicates that it too is organized on a scale that largely mirrors this scale of PW variability. Clearly, the scale of organization of convection is dramatically influenced by the dimensionality of the model, and determining reasons for this difference in scale is a topic of ongoing research.

Further basic characteristics of the wet and dry regions, beyond those presented in Figs. 3 and 4, are summarized in Table 2. This table presents selected properties of the equilibrium state grouped into three regimes according to the simulated OLR using the following OLR thresholds: (i) a low-OLR regime that characterizes deep convection as typified by heavy precipitation and the presence of thick ice clouds, (ii) an intermediate-OLR regime that characterizes “cumulus convection,” which primarily consists of (precipitating) water clouds relatively free of ice, and (iii) a high-OLR regime that identifies mostly “clear skies” that are devoid of most cloud but not entirely so. Regions defined in this way do not entirely isolate the effects of deep convection from shallow convection and clear-sky regions. Regions of deep convection and thick anvil cloud in the moist regions, for instance, also contain shallow convection below, and the regions of shallow convection are furthermore juxtaposed with clear regions in

such a way that the evaporation from these neighboring clear regions is strongly influenced by the local-scale turbulence associated with the shallow convection. Nevertheless, compositing the results of experiments in this way reveals much about the hydrological processes at equilibrium. Listed in Table 2 are the percentage contributions of these three cloud regimes to the total cloud water path (CWP), ice water path (IWP), surface latent heat flux (LH), and precipitation for both control experiments and the 2D and 3D versions of the radiation perturbation experiment (FIXRAD); the results for the NO-OPTICS experiments are not included since there is no contribution to the OLR by clouds in these experiments by design. The quantities summarized indicate that the clear-sky and cumulus regimes combined contribute between 76% and 89% of all the latent heating and thus surface moistening over the entire model domain. These regimes also lose between 13% and 28% of this moisture by shallower modes of precipitation. Conversely, evaporation in designated regions of deep convection contributes between 11% and 24% to the total water content of the domain, whereas these regions account for 72%–87% of the moisture lost by precipitation. The final equilibrium state of the FIXRAD appears to be at variance with these results, with 58% of the evaporation occurring in regions designated as “deep convective.” However, this merely reflects the greater coverage of thick cirrus produced in these experiments relative to the control and the regions of these thicker clouds overlying shallower convection that are thus misinterpreted through the OLR threshold as deep convection.

5. Mean profile structures at equilibrium

The domain-averaged characteristics of the 2D and 3D equilibrium states are further examined in Figs. 5–7 to demonstrate other important characteristics of the equilibria. Shown in Fig. 5 are the vertical temperature and moisture profiles in the form of a skew T -log P thermodynamic chart (Fig. 5a), the relative humidity (Fig. 5b), the cloud fraction (where cloud is assumed to exist above the condensate threshold noted earlier; Fig. 5c), and the averaged profile of the condensate mixing ratio (Fig. 5d) for the control experiments averaged over days 46–49. The net radiative heating profiles averaged over days 45–49 and also over the entire domain and over the undisturbed and disturbed portions of the domain as defined above are shown in Figs. 6a, 6b, and 6c respectively for the control experiments. Figure 7 provides similar profiles of the domain-averaged radiative heating (Figs. 7a and 7b) and cloud cover (Figs. 7c and 7d) for the CONTROL, NO-OPTICS, and

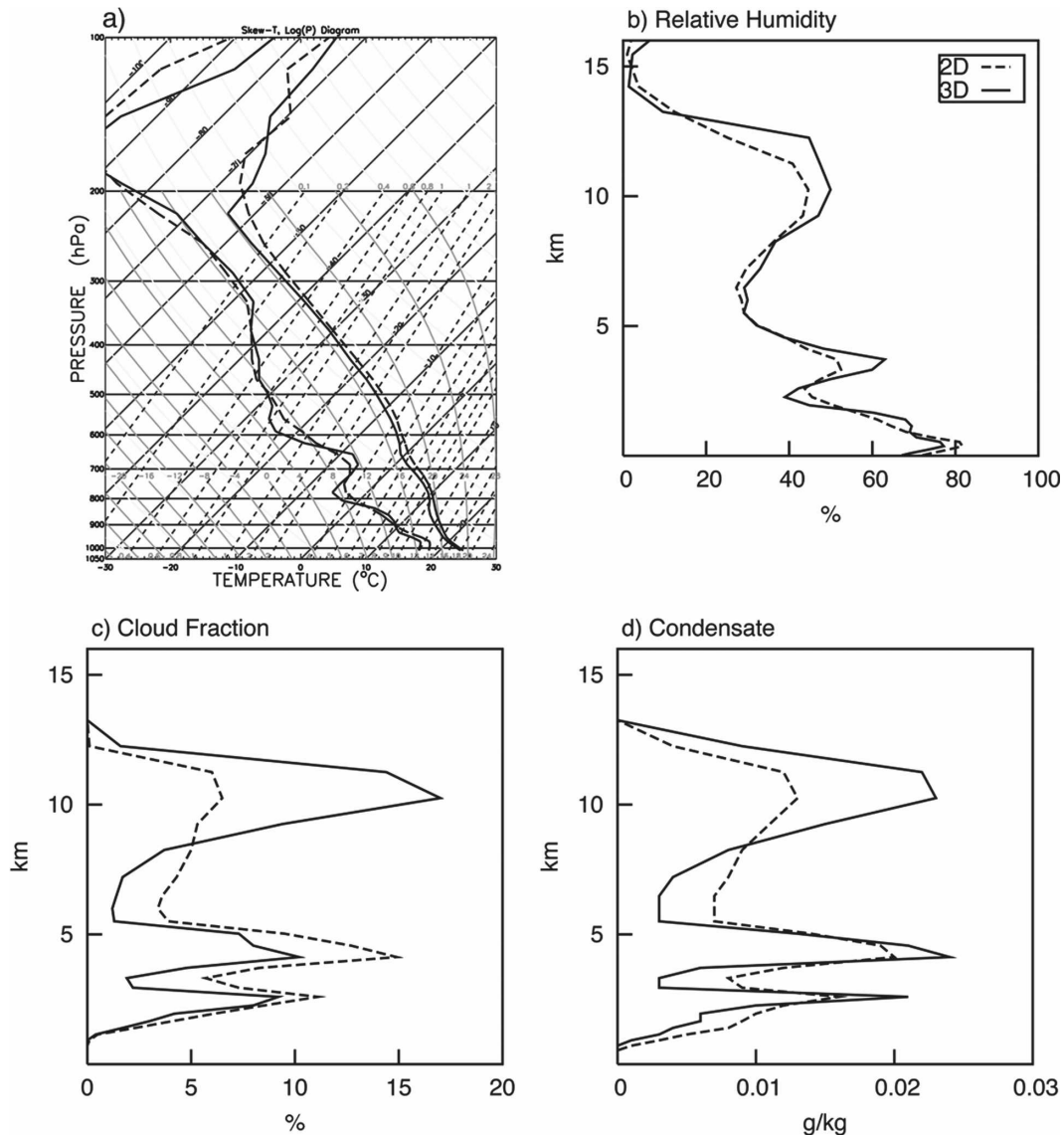


FIG. 5. (a) The temperature and dewpoint temperatures expressed in the form of a skew- T diagram. (b)–(d) The vertical profile of (b) relative humidity (%), (c) cloud fraction, and (d) condensate mixing ratio. All profiles are derived from averages of days 45–49 of the control experiments.

FIXRAD versions of the 2D and 3D experiments from days 45–49. The cloud cover for days 90–94 of all four 2D experiments is presented in Fig. 7e. Relevant features of these figures include the following:

- (i) The time-domain average temperature and moisture structures (Fig. 5a) and the differences between the 2D and 3D control experiments, in particular, resemble the results of Tompkins (2000). Above about 650 hPa, the temperature follows a moist adiabat. The moisture profile, on the whole, reflects the presence of a trimodal cloud vertical

- structure, as discussed below. The warmer and moister boundary layer of the 2D experiment is noted by Tompkins (2000), who explained the difference in terms of the response of the atmosphere to an idealized point buoyancy source. Bretherton and Smolarkiewicz (1989) show that the 2D response in the adjustment region of the spreading gravity wave involves a constant velocity everywhere, whereas the outflow velocity in the 3D response decreases inversely with radius.
- (ii) The vertical distributions of cloud amount (Fig. 5c) and condensate (Fig. 5d) are distinctly trimodal,

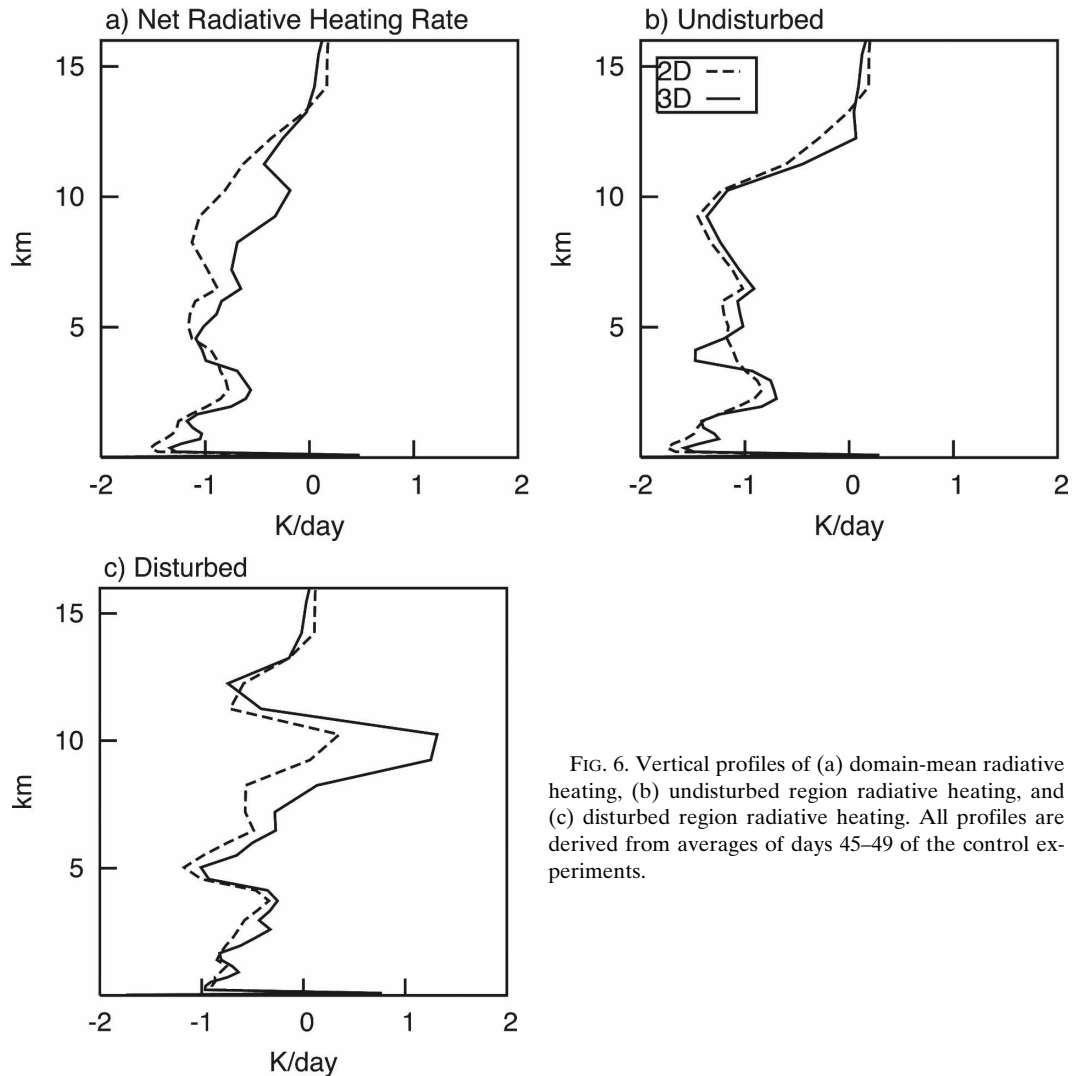


FIG. 6. Vertical profiles of (a) domain-mean radiative heating, (b) undisturbed region radiative heating, and (c) disturbed region radiative heating. All profiles are derived from averages of days 45–49 of the control experiments.

with peaks occurring at 2–3 km, just below 5 km, and in the upper troposphere slightly above 10 km. This trimodal structure is also reflected in the relative humidity profiles (Fig. 5b) and has a broad resemblance to reality (e.g., Johnson et al. 1999 and Haynes and Stephens 2007), although there are some differences in detail. For example, the middle peak of the model simulations falls below the 6–8-km level apparent in the CloudSat observations reported by Haynes and Stephens (2007). The latter results apply to a composite of observations over a range of SSTs and thus over a range of profiles in which the melting level varies. The second mode of clouds in the model simulations occurs at and near the melting and is much more pronounced in these simulations than in reality for reasons alluded to in Posselt et al. (2008). Also noteworthy are the significantly larger amounts of upper tropospheric

cloudiness in the 3D control compared to the 2D control experiment (Figs. 5c, 5d, and 7). This difference is associated with differences in cloud-scale vertical motions described in the next section. The vertical distribution of cloudiness for the three sensitivity experiments also reveals marked changes in high-level cloudiness compared to the respective control experiments. The NO-OPTICS experiment produces substantial increases of high clouds from the beginning (relative to the control), whereas the high clouds of the FIXRAD experiment are reduced initially (Figs. 7c and 7d) but eventually increase over time to a point where the high cloud amount of both the FIXRAD and NO-OPTICS sensitivity experiments are substantially increased over that of the control. For example, the maximum cloud amount occurs near 10 km and exceeds 60% in both experiments. The amount of high

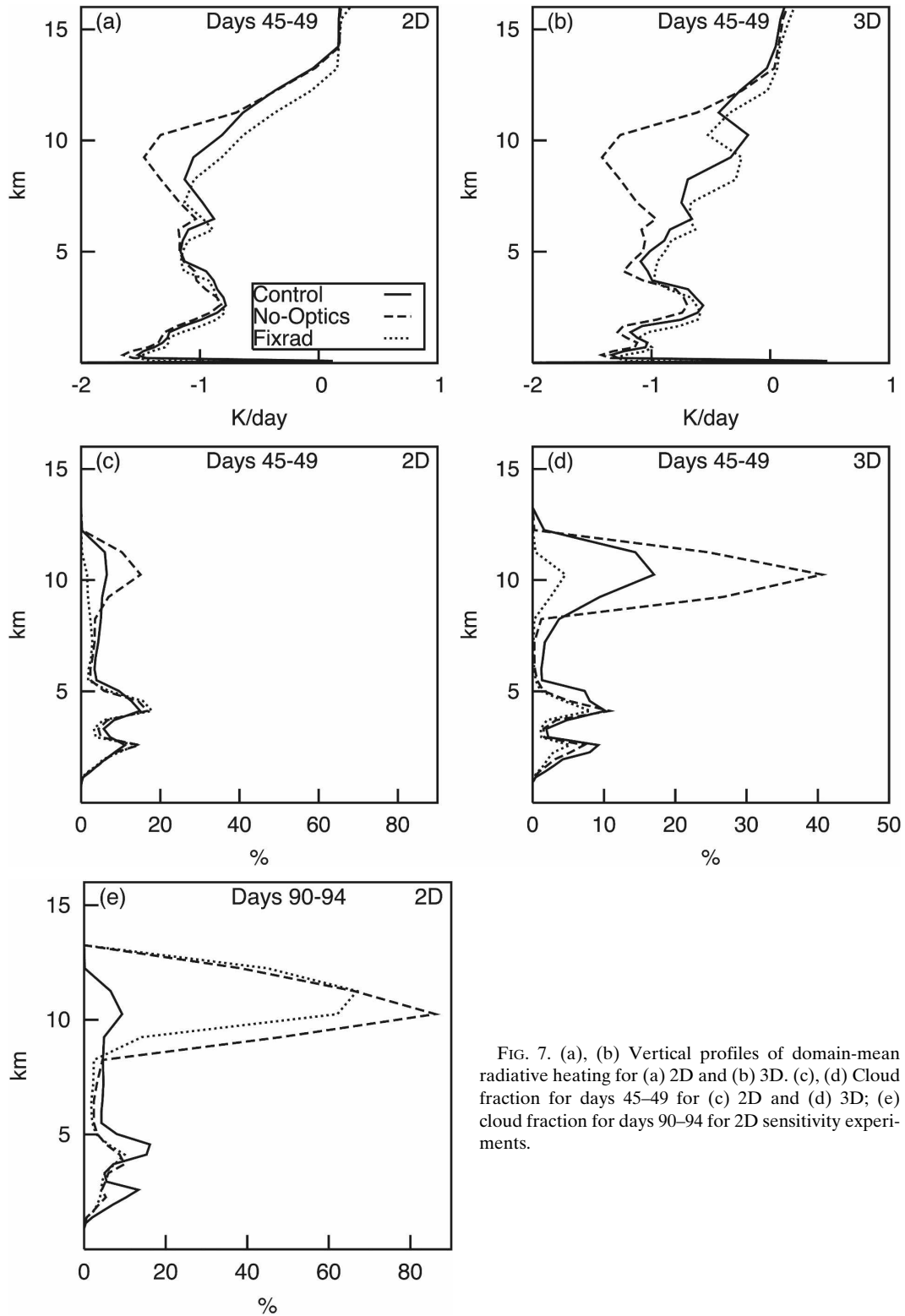


FIG. 7. (a), (b) Vertical profiles of domain-mean radiative heating for (a) 2D and (b) 3D. (c), (d) Cloud fraction for days 45–49 for (c) 2D and (d) 3D; (e) cloud fraction for days 90–94 for 2D sensitivity experiments.

cloud of the ANVIL experiment, by contrast, is similar to the control, with a maximum high cloud amount also occurring near 10 km but with an amount that is only about 10% in both experiments.

- (iii) There is less domain-mean radiative cooling of the upper troposphere in the disturbed regions of the control experiments (Fig. 6c) than in the undisturbed portions of the domain (Fig. 6b). This is due to the localized radiative effects of high clouds in the disturbed regions that heat the upper troposphere mostly at the bases of high thick clouds with cooling from their tops (e.g., Stephens 1980) and is the basic source of the moist-dry radiative heating gradients. The undisturbed heating profiles of the 2D and 3D experiments are similar to each other because these are largely defined by clear-sky temperature and moisture profiles, which are much less dependent on the dimensionality of the model. The heating by high clouds is also more pronounced in the 3D control experiment owing to the increased amounts of upper tropospheric clouds in that experiment (Fig. 6c). Radiative cooling from the tops of the two shallower modes of convection near 2 km and 5 km produce slightly increased amounts of cooling at these cloud-top levels. (4) Comparison of the three sensitivity experiments to the control (Figs. 7a–c) shows significantly more radiative cooling in the upper troposphere of both the 2D and 3D NO-OPTICS experiments than the CONTROL, FIXRAD, or ANVIL experiments. This enhanced upper-tropospheric domainwide cooling is, by construction, a result of the lack of high-cloud radiative heating in the NO-OPTICS experiments.

6. Cloud mass fluxes

Convective mass fluxes and other associated properties also offer much insight into the bulk nature of convection. The upward cloud mass flux (M) and the convective mass flux (M_c) were computed at each model level as (e.g., Robe and Emanuel 1996)

$$M = \frac{\rho}{N} \sum_{q_c > q_o, w > 0} w_{i,j} = \rho \bar{w} \sigma, \quad (1)$$

where ρ is the air density and N is the total number of grid points. The summation is over the total number of grid points (N_c grid points) for which the vertical velocity is upward. The cloudy grid points are those previously identified as the disturbed regions determined by the abovementioned water path threshold; σ is therefore the cloud fraction with upward motion (equal

to the ratio N_c/N). The convective mass flux M_c , the corresponding mean convective velocity w_c , and the coverage area σ_c are defined in the same way, with the summation performed only over those cloudy grid points for which $w > 1 \text{ m s}^{-1}$, broadly consistent with the specification of convection of LeMone and Zipser (1980).

Time- and domain-averaged vertical profiles of the convective mass fluxes are shown in Fig. 8 for the control experiments. As expected, the 2D and 3D mass flux distributions for both control experiments are similar to each other (Fig. 8a) because these profiles are broadly (but not entirely) dictated by the structure of the radiative cooling profiles (Figs. 6 and 7). The convective updraft velocity w_c , however, is significantly larger in the case of 3D convection (Fig. 8b), which presumably influences the amount of cloud ice detrained at upper levels and thus the larger higher cloud amounts observed in the 3D experiment (Fig. 5c). This feature of 3D updrafts is also noted in the study of Phillips and Donner (2006). The maximum convective mass flux in the lower levels of both experiments reflects both the maximum low-level radiation (Stephens and Wilson 1980) and low-level evaporation at these levels (Emanuel 1994). We remark, however, that reference here to shallow convection is done loosely because the model does not resolve such convection on the scale typical of such convection in the real world. The shallow cloudiness that develops at these lower levels in the model is a surrogate form of shallow convection, presumably playing a role similar to real shallow convection.

The convective mass fluxes for days 45–49 are presented in Figs. 9a and 9b for the 2D and 3D CONTROL, FIXRAD, and NO-OPTICS experiments. Convective mass fluxes are increased throughout the troposphere below 10 km in the NO-OPTICS experiments relative to the control but are decreased at all levels early in the integration of the FIXRAD experiments (days 45–49). The explanation for this partially resides in the fact that significantly more radiative cooling occurs in the upper troposphere of both the 2D and 3D NO-OPTICS experiments compared to either the CONTROL or the FIXRAD experiments, requiring increased convective mass fluxes to balance the increased mass of subsiding air driven by the enhanced radiative cooling of this experiment. The convective fraction areas and convective mass fluxes for all 2D experiments are shown in Figs. 9c and 9d respectively for days 90–94. In this case, the convective mass fluxes of the FIXRAD experiment have now increased relative to the control and lie between this and the NO-OPTICS experiments. Again, the ANVIL and CONTROL convective mass fluxes and fractional areas are similar to each other.

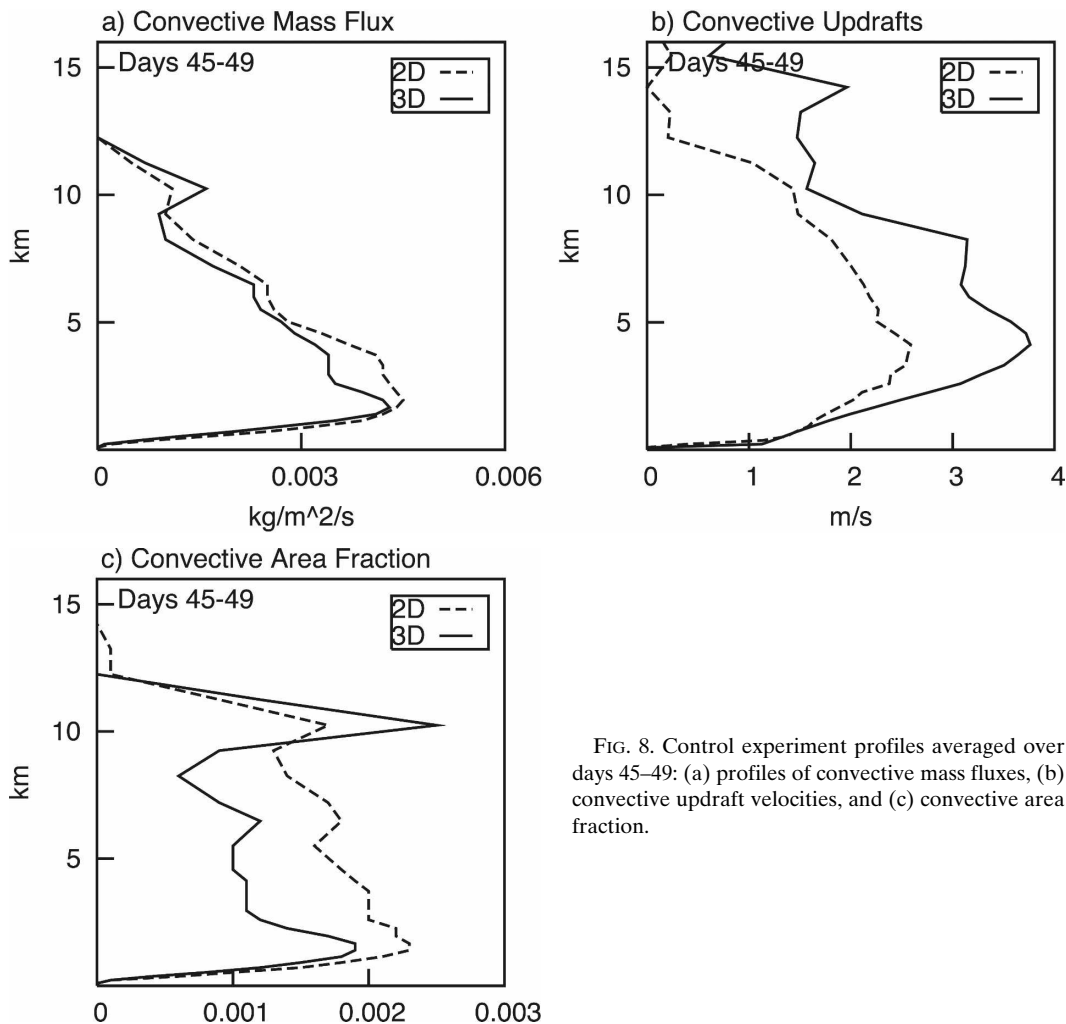


FIG. 8. Control experiment profiles averaged over days 45–49: (a) profiles of convective mass fluxes, (b) convective updraft velocities, and (c) convective area fraction.

7. Summary and discussion

The topic of this paper concerns the role of radiation and its interaction with clouds and convection in defining the state of radiative–convective equilibrium and the effects of radiation in shaping and organizing convection on time scales pertinent to RCE. This paper describes the results of numerical RCE experiments conducted using both 2D and 3D versions of a cloud-resolving model aimed at exploring the importance of feedbacks between convection and cloud–radiation interactions in such systems.

The state of equilibrium that developed in the control experiments reported in this paper resembles that of other studies of this type, namely, one of alternating regions of dry and moist air distributed across the domain. Although the equilibria attained quantitatively differ between the 2D and 3D experiments, much about these equilibria and the feedbacks related to radiative

processes are shown to be similar. Equilibria in both cases develop as juxtaposed regions of dry and moist air that are connected by circulations between them. The moist regions are fed by the dry regions where most of the low-level moistening occurs (Table 2), and the dry regions in turn are established by the broad-scale subsidence required for mass balance with upward motions in the convective regions. Thus, a circulation is formed between these wet and dry areas that in large part reinforces each region. The scales of this wet–dry circulation exceed 1000 km in 3D and 2000 km in 2D.

It also follows from the sensitivity experiments performed that radiation feedbacks are responsible for the wet–dry state of equilibrium achieved in the control and that two important mechanisms govern this equilibrium and the convection that forms within it:

- (i) The bimodal nature of the moist equilibrium is largely established by gradients of radiative heating

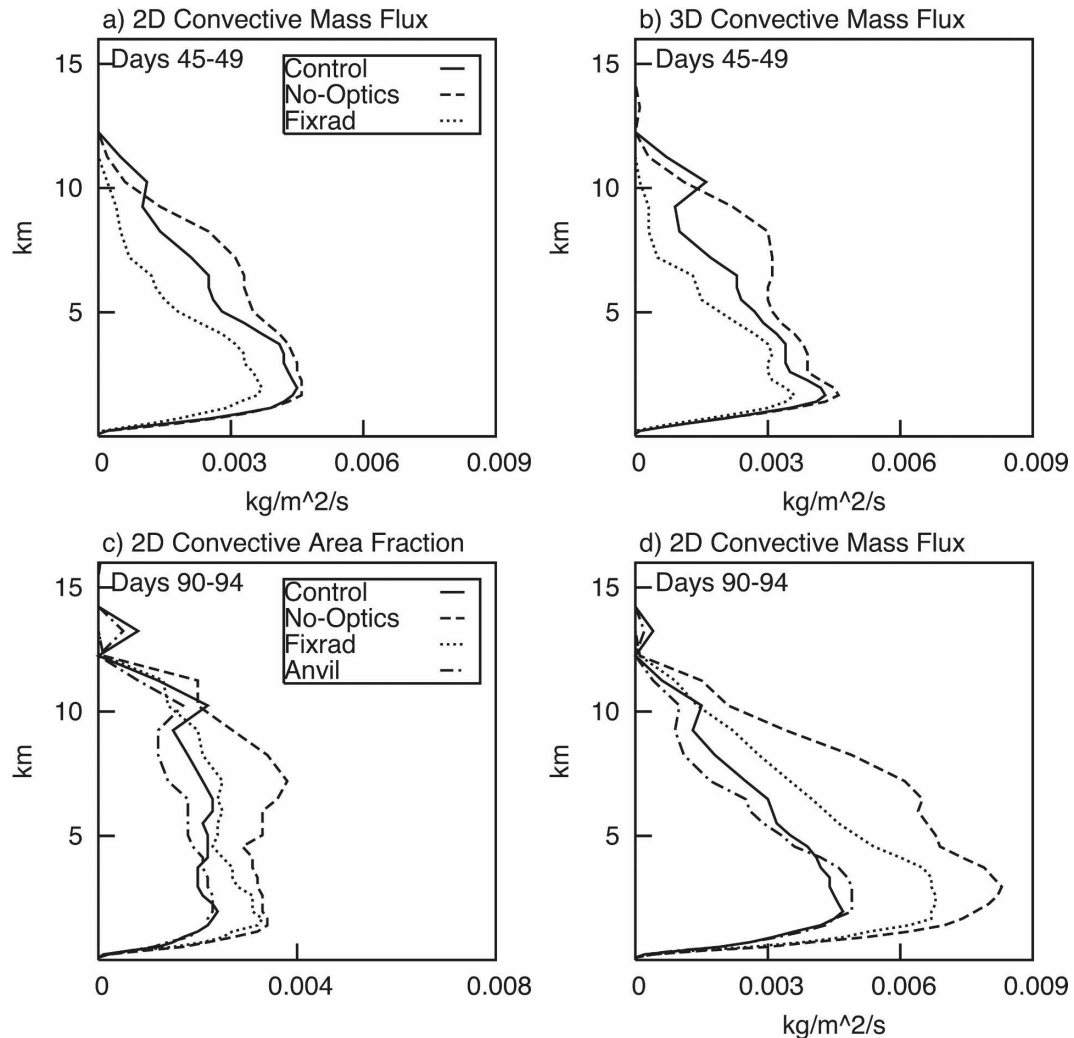


FIG. 9. Domain-mean profiles from the sensitivity experiments. (a) Profiles of convective mass fluxes derived from the average of days 45–49 of the 2D control and 2D FIXRAD and NO-OPTICS experiments. (b) As in (a), but for the 3D experiments. (c) Convective area fraction and (d) convective mass flux, both for the 2D control and the 3 sensitivity experiments averaged over days 90–94.

that, in turn, are determined by cloud differences between wet and dry regions that, in turn, are controlled by convection. The principal factor that establishes these gradients is the high clouds of the wet areas (and the lack of high clouds in dry areas). When these radiative heating gradients are removed, the quasi-stationary regions of moisture and convection no longer occur, and convection now propagates in both directions with speeds of approximately $15\text{--}20\text{ m s}^{-1}$. The lack of this quasi-stationary structure in the NO-OPTICS experiments (in which the gradients in radiative heating are established only by water vapor variations) indicates these heating gradients are too weak to act as a source of feedback on the organization of

moisture and convection. These results are consistent with other studies (e.g., Grabowski and Moncrieff 2001, 2002; Bony and Emanuel 2005), and why systems propagate in the absence of radiation feedbacks is a topic of an ongoing study. The fact that both the FIXRAD and NO-OPTICS experiments eventually evolve to an equilibrium state that is similar in nature (e.g., Fig. 3) merely reinforces the claim that the differential radiative heating between convectively disturbed moist areas and drier convectively suppressed areas results from cloud–radiation differences that exert a controlling influence on the strength of the self-sustaining circulation between these regions. This result supports the findings of others, such as Raymond (2000) and

Bretherton et al. (2005), among others. The fact that the ANVIL experiment resembles so closely the control experiment points to the radiative effects of high clouds as the principal contributor to these heating gradients.

- (ii) The radiative heating gradients are importantly set by the amount of high clouds detrained from convection. This radiative heating by high anvil clouds connected to the convection within the wet areas also provides a more direct feedback on convection in a way that regulates the amount of high cloud. The lack of a localized upper-tropospheric radiative heating by these clouds in both the FIXRAD and NO-OPTICS experiments influences the stability of the atmosphere in such a way that convection is strengthened (e.g., larger mass fluxes in Fig. 9c), thereby producing more high clouds relative to the control experiments (Fig. 7g). In fact, the high clouds increase by a factor of 6–8 over the control high cloud amount. When the radiative heating by these upper level clouds is included as in both the CONTROL and ANVIL experiments, the fraction of high cloudiness is significantly reduced despite the fact that the fractional areas of convection are not greatly reduced (at least compared to the FIXRAD experiment). These experiments thus demonstrate how high cloud radiative heating, a by-product of the convection itself, provides a feedback that acts to regulate the high clouds produced in the wet convective areas, much in the stabilization mode visualized in the study of Stephens et al. (2004). The regulation of high cloudiness through the effects of radiative heating on convection has also been noted in a number of other studies, such as in the global model study of Fowler and Randall (1994).

Acknowledgments. Much of the research of the lead author on cloud climate feedbacks is supported under the U.S. Department of Energy, Office of Science, Office of Biological and Environmental Research, Environmental Sciences Division under Grant DE-FG03-94ER61748 as part of the Atmospheric Radiation Measurement (ARM) Program. Other support for this research was provided by the NOAA grant under NOAA cooperative agreement NA17RJ1228.

REFERENCES

- Arakawa, A., 2004: The cumulus parameterization problem: Past, present, and future. *J. Climate*, **17**, 2493–2525.
- Bony, S., and K. A. Emanuel, 2005: On the role of moist processes in tropical intraseasonal variability: Cloud–radiation and moisture–convection feedbacks. *J. Atmos. Sci.*, **62**, 2770–2789.
- Bretherton, C. S., and P. K. Smolarkiewicz, 1989: Gravity waves, compensating subsidence, and detrainment around cumulus clouds. *J. Atmos. Sci.*, **46**, 740–759.
- , P. N. Blossey, and M. Khairoutdinov, 2005: An energy-balance analysis of deep convective self-aggregation above uniform SST. *J. Atmos. Sci.*, **62**, 4273–4292.
- Bryan, G. H., J. C. Wyngaard, and J. M. Fritsch, 2003: Resolution requirements for the simulation of deep moist convection. *Mon. Wea. Rev.*, **131**, 2394–2416.
- Cotton, W. R., and Coauthors, 2003: RAMS 2001: Current status and future directions. *Meteor. Atmos. Phys.*, **82**, 5–29.
- Dudhia, J., 1989: Numerical study of convection observed during the winter monsoon experiment using a mesoscale two-dimensional model. *J. Atmos. Sci.*, **46**, 3077–3107.
- Emanuel, K. A., 1994: *Atmospheric Convection*. Oxford University Press, 580 pp.
- Fowler, L., and D. A. Randall, 1994: A global radiative–convective feedback. *Geophys. Res. Lett.*, **21**, 2035–2038.
- Fu, Q., S. K. Krueger, and K. N. Liou, 1995: Interactions of radiation and convection in simulated tropical cloud clusters. *J. Atmos. Sci.*, **52**, 1310–1328.
- Grabowski, W. W., and M. W. Moncrieff, 2001: Large-scale organization of tropical convection in two-dimensional explicit numerical simulations. *Quart. J. Roy. Meteor. Soc.*, **127**, 445–468.
- , and —, 2002: Large-scale organization of tropical convection in two-dimensional explicit numerical simulations: Effects of interactive radiation. *Quart. J. Roy. Meteor. Soc.*, **128**, 2349–2375.
- , and —, 2004: Moisture–convection feedback in the tropics. *Quart. J. Roy. Meteor. Soc.*, **130**, 3081–3104.
- Gray, W. M., and R. W. Jacobson, 1977: Diurnal variation of deep cumulus convection. *Mon. Wea. Rev.*, **105**, 1171–1188.
- Harrington, J. Y., 1997: The effects of radiative and microphysical processes on simulated warm and transition season Arctic stratus. Ph.D. dissertation, Colorado State University, 289 pp. [Available from Department of Atmospheric Science, Colorado State University, Fort Collins, CO 80523.]
- Haynes, J. M., and G. L. Stephens, 2007: Tropical ocean cloudiness and the incidence of precipitation: Early results from CloudSat. *Geophys. Res. Lett.*, **34**, L09811, doi:10.1029/2007GL029335.
- Held, I. M., R. S. Hemler, and V. Ramaswamy, 1993: Radiative–convective equilibrium with explicit two-dimensional moist convection. *J. Atmos. Sci.*, **50**, 3909–3927.
- Hill, G. E., 1974: Factors controlling the size and spacing of cumulus clouds as revealed by numerical experiments. *J. Atmos. Sci.*, **31**, 646–673.
- Johnson, R. H., T. M. Rickenbach, S. A. Rutledge, P. E. Ciesielski, and W. H. Schubert, 1999: Trimodal characteristics of tropical convection. *J. Climate*, **12**, 2397–2418.
- Kiehl, J. T., and K. E. Trenberth, 1997: Earth’s annual global mean energy budget. *Bull. Amer. Meteor. Soc.*, **78**, 197–208.
- LeMone, M. A., and E. J. Zipser, 1980: Cumulonimbus vertical velocity events in GATE. Part I: Diameter, intensity, and mass flux. *J. Atmos. Sci.*, **37**, 2444–2457.
- Lilly, D. K., 1962: On the numerical simulation of buoyant convection. *Tellus*, **14**, 148–172.
- Louis, J.-F., 1979: A parametric model of vertical eddy fluxes in the atmosphere. *Bound.-Layer Meteor.*, **17**, 187–202.
- , M. Tiedtke, and J. F. Geleyn, 1981: A short history of the operational PBL parameterization at ECMWF. *Proc. Workshop on Planetary Boundary Layer Parameterization*, Read-

- ing, United Kingdom, European Centre for Medium-Range Weather Forecasts, 59–79.
- Mapes, B., 2001: Water's two height scales: The moist adiabat and the radiative troposphere. *Quart. J. Roy. Meteor. Soc.*, **127**, 2353–2366.
- Meyers, M. P., R. L. Walko, J. Y. Harrington, and W. R. Cotton, 1997: New RAMS cloud microphysics parameterization. Part II: The two-moment scheme. *Atmos. Res.*, **45**, 3–39.
- Mitchell, J. F. B., C. A. Wilson, and W. M. Cunnington, 1987: On CO₂ climate sensitivity and model dependence of results. *Quart. J. Roy. Meteor. Soc.*, **113**, 293–322.
- Phillips, V. T., and L. J. Donner, 2006: Cloud microphysics, radiation, and vertical velocities in two- and three-dimensional simulations of deep convection. *Quart. J. Roy. Meteor. Soc.*, **132**, 3011–3033.
- Pielke, R. A., and Coauthors, 1992: A comprehensive meteorological modeling system—RAMS. *Meteor. Atmos. Phys.*, **49**, 69–91.
- Posselt, D. J., S. C. van den Heever, and G. L. Stephens, 2008: Trimodal cloudiness and tropical stable layers in simulations of radiative–convective equilibrium. *Geophys. Res. Lett.*, **35**, L08802, doi:10.1029/2007GL033029.
- Raymond, D. J., 2000: The Hadley circulation as a radiative–convective instability. *J. Atmos. Sci.*, **57**, 1286–1297.
- Robe, F. R., and K. A. Emanuel, 1996: Dependence of tropical convection on radiative forcing. *J. Atmos. Sci.*, **53**, 3265–3275.
- Sherwood, S. C., 1999: Feedbacks in a simple prognostic tropical climate model. *J. Atmos. Sci.*, **56**, 2178–2200.
- Smagorinsky, J., 1963: General circulation experiments with the primitive equations. Part I: The basic experiment. *Mon. Wea. Rev.*, **91**, 99–164.
- Stephens, G. L., 1980: Radiative properties of cirrus clouds in the infrared region. *J. Atmos. Sci.*, **37**, 435–446.
- , 1990: On the relationship between water vapor over the oceans and sea surface temperature. *J. Climate*, **3**, 634–645.
- , 2005: Cloud feedback in the climate system: A critical review. *J. Climate*, **18**, 237–273.
- , and K. J. Wilson, 1980: The response of a deep cumulus convection model to changes in radiative heating. *J. Atmos. Sci.*, **37**, 421–434.
- , P. J. Webster, R. H. Johnson, R. Engelen, and T. L'Ecuyer, 2004: Observational evidence for the mutual regulation of the tropical hydrological cycle and tropical sea surface temperatures. *J. Climate*, **17**, 2213–2224.
- Su, H., C. Bretherton, and S. S. Chen, 2000: Self-aggregation and large-scale control of tropical deep convection: A modeling study. *J. Atmos. Sci.*, **57**, 1797–1816.
- Tao, W.-K., S. Lang, J. Simpson, C.-H. Sui, B. Ferrier, and M.-D. Chou, 1996: Mechanisms of cloud–radiation interaction in the tropics and midlatitudes. *J. Atmos. Sci.*, **53**, 2624–2651.
- , J. Simpson, C.-H. Sui, C.-L. Shie, B. Zhou, K. M. Lau, and M. Moncrieff, 1999: Equilibrium states simulated by cloud-resolving models. *J. Atmos. Sci.*, **56**, 3128–3139.
- Tompkins, A. M., 2000: The impact of dimensionality on long-term cloud-resolving model simulations. *Mon. Wea. Rev.*, **128**, 1521–1535.
- , 2001: Organization of tropical convection in low vertical wind shears: The role of water vapor. *J. Atmos. Sci.*, **58**, 529–545.
- , and G. C. Craig, 1998a: Radiative–convective equilibrium in a three-dimensional cloud-ensemble model. *Quart. J. Roy. Meteor. Soc.*, **124**, 2073–2097.
- , and —, 1998b: Time scales of adjustment to radiative–convective equilibrium in the tropical atmosphere. *Quart. J. Roy. Meteor. Soc.*, **124**, 2693–2713.
- Tulich, S., D. A. Randall, and B. E. Mapes, 2007: Vertical-mode and cloud decomposition of large-scale convectively coupled gravity waves in a two-dimensional cloud-resolving model. *J. Atmos. Sci.*, **64**, 1210–1229.
- Walko, R. L., W. R. Cotton, M. P. Meyers, and J. Y. Harrington, 1995: New RAMS cloud micro-physics parameterization. Part I: The single-moment scheme. *Atmos. Res.*, **38**, 29–62.
- , and Coauthors, 2000: Coupled atmosphere–biophysics–hydrology models for environmental modeling. *J. Appl. Meteor.*, **39**, 931–944.
- Webster, P. J., and G. L. Stephens, 1980: Tropical upper-tropospheric extended clouds: Inferences from winter MONEX. *J. Atmos. Sci.*, **37**, 1521–1541.
- Xu, K.-M., and D. A. Randall, 1995: Impact of interactive radiative transfer on the macroscopic behavior of cumulus ensembles. Part II: Mechanisms for cloud–radiation interactions. *J. Atmos. Sci.*, **52**, 800–817.